Journal of Crystal Growth 417 (2015) 16–24

Contents lists available at ScienceDirect

Journal of Crystal Growth

journal homepage: www.elsevier.com/locate/jcrysgro

Axial vibration control of melt structure of sodium nitrate in crystal growth process

Andrey Sadovskiy, Ekaterina Sukhanova, Stanislav Belov, Vladimir Kostikov, Marina Zykova, Maxim Artyushenko, Evgeny Zharikov, Igor Avetissov *

Mendeleyev University of Chemical Technology of Russia, Chair of Crystal Chemistry and Technology, Miusskaya pl.9, 125047, Moscow, Russian Federation

ARTICLE INFO

Available online 12 January 2015

Keywords:
Computer simulation
Mass transfer
Convection
Growth from melt

ABSTRACT

The melt structure evolution under the action of the low-frequency axial vibration control (AVC) technique was studied *in situ* by Raman spectroscopy for several complex chemical compound melts: sodium nitrate, margarine acid, paraffin mixture (C_{17}-C_{20}). The measurements were conducted in the temperature range from the melting point up to 60 °C above. Comparison of crystallization heats for AVC activated and steady melts with melting heats of AVC-CZ and conventional CZ produced powders allowed to propose the energy diagram of $NaNO_3$ states for activated and non-activated melts and crystals based on DTA, XRD, DSC and Raman experimental data.

1. Introduction

The problem of the effective heat-mass transfer in melt-crystal growth technologies plays a significant role in production of high quality crystals. The fluid flow can modify the effective segregation at the interface, producing macro-segregation with adverse effect (striations in crystals, increase of dopant level during growth). To control heat-mass transfer in melt-crystal growth a number of techniques was successfully applied for the past 20 years (see review [1] and references therein). Among these techniques the low-frequency axial vibration control (AVC) technique demonstrated enviable perspectives for its universe application to efficient heat mass transfer in Bridgman, CZ, VGF and other melt-growth techniques as well as crystal quality enhancement [2].

Structural changes and alteration of properties in material during the melting process and after that are supporting the idea of heritage between solid and liquid phase [3]. It may be said that the melt at a temperature range closed to the melting point has a structure more similar to the solid phase, then to the gas phase [4]. The more distinctly this situation is observed in case of thermotropic liquid crystal materials [5]. Nowadays, the melt structure of pure metals and metal alloys are more studied in detail [6]. For complex inorganic compounds one of the most studied melts are borates investigated by high temperature Raman spectroscopy [7]. In case of complex semiconductors ($A^{III}B^{V}$, $A^{II}B^{VI}$) the structural changes vary significantly but to the moment there are no reliable data on structures of complex semiconductors melts and pathways to control them.

In the present research we tried to prove the hypothesis about the AVC technique as an efficient instrument for structure control of melts of complex chemical compounds of different nature.

2. Experiment techniques

2.1. Raman spectra experiments

To prove the hypothesis about AVC-melt dissociation we analyzed sodium nitrate melt by Raman spectroscopy.

2.1.1. Raman cell

A setup for Raman spectrum measurements of melt activated by AVC was designed (Fig. 1). We made an isothermal aluminum cell, in which the AVC was induced in melt by a quartz glass disk oscillation.

The specific feature of the setup is 0.2 mm quartz glass window for Raman measurements in geometry of photon backscattering. Raman spectra were obtained using Ocean Optics QE6500 spectrometer supported by 785 nm excitation laser and optical fiber cable for input/output of light signal. Integration time was 30 s for the every run in the range 200–2000 cm^{-1}. It was enough to collect Raman photons at 500–1000 mW laser pumping power and to avoid the Raman probe overheating. The laser beam was focused in 7.5 mm distance from the probe output window and the focus point was in the melt in the middle between the quartz window and the oscillating disk (Fig. 2 point #1). The laser beam passed

* Corresponding author. Tel.: +7 495 4966177.
E-mail address: igor_avetisov@mail.ru (I. Avetissov).

http://dx.doi.org/10.1016/j.jcrysgro.2014.11.022
0022-0248/

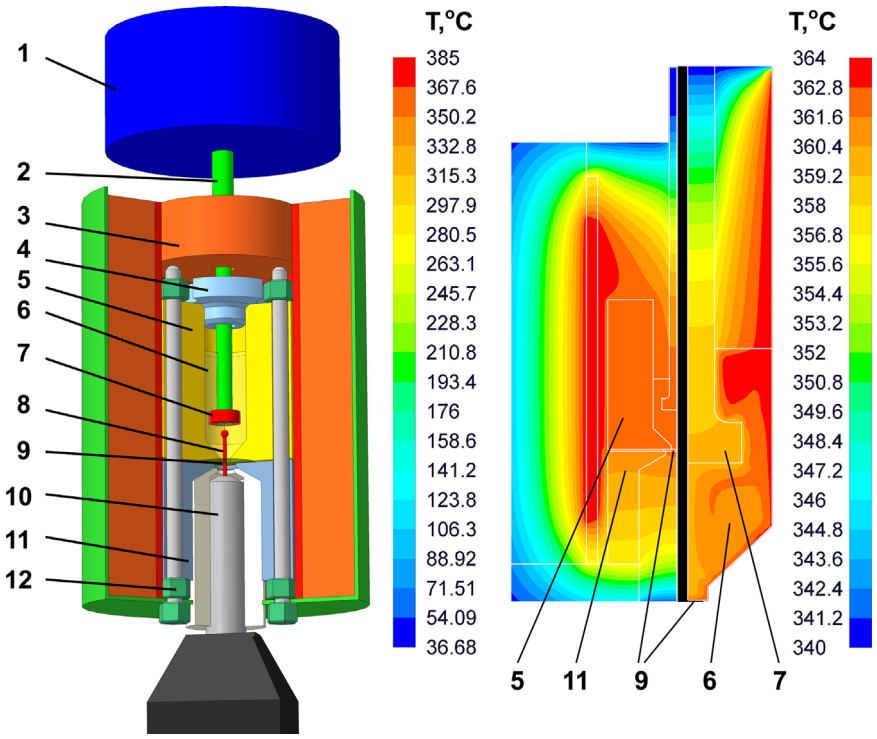

Fig. 1. Scheme of setup for Raman measurements of the melt, activated by AVC (left) and temperature distribution into the cell (right). 1-vibrational mechanism, 2-rod, 3-kaolin wool thermoinsulating cover, 4-aluminium cover, 5-cell body, 6-melt, 7- oscillating baffle, 8- laser beam, 9-quartz glass window, 10- Raman probe, 11- body face, 12-screw.

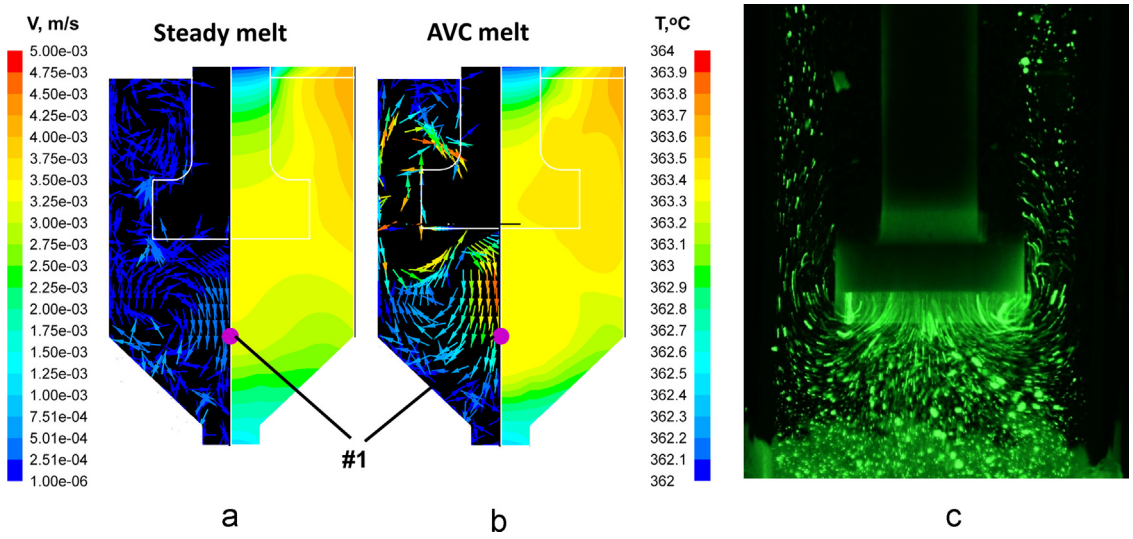

Fig. 2. Distributions of velocity vectors (left-hand side) and temperature (right-hand side) for steady (*a*), AVC activated ($\boldsymbol{A}$=0.7 mm and $\boldsymbol{f}$=25 Hz) $NaNO_3$ melt (*b*) and experimental flow's picture (*c*). The point #1 shows the position of the laser focus of the Raman probe.

through 4 mm melt/solid layer. The spot diameter was 0.3 mm. Thus the power density of laser emission in the point was as high as 110 kW/cm^2.

We checked the influence of quartz glass on a Raman spectrum by measurements the spectra through the glass and from the free surface and found out that in the temperature range 25 °C to 324 °C for solid/liquid $NaNO_3$ (see Suppl.), margarine acid and paraffin mixture the spectra were identical.

2.1.2. *Numerical simulation*

Experimental cell for Raman-spectrum measurements (Fig. 1) has been numerically analyzed with ANSYS 14.5 Fluent software. 2D geometry for two cases, one including the cell and the furnace and the other inner volume of the cell with the melt, gas and vibrating baffle, has been covered with tetrahedral cells of 0.2 mm general size. To obtain the solution for the temperature distribution and flow field in the melt the Pressure Based solver (Boussinesq approximation) with PISO pressure-velocity coupling scheme has been used in the case of enable vibrations and for thermal conductivity in solid zones - standard FLUENT equations set [8]. As initial boundary conditions constant temperature on the heating zone and convective heat transfer with ambient temperature 25 °C on outer walls has been applied. Physical properties for all applied materials are summarized in Table 1.

To visualize the flow's patterns in case of margarine acid and paraffin mixture we used a transparent cell made from quartz glass similar to that was described in Ref. [9]. According to

Table 1
Material properties for numerical simulation [15–17].

Property	Sodium nitrate (melt)	Air	Kaolin- wool	Quartz glass	Al
Density, ρ (kg/m^3)	1903	0.33	1.225	2201	2700
Thermal conductivity, λ (W/m × K)	2.5×10^{-3}	0.0242	0.16	1.38	20
Specific heat, C_p (J/kg × K)	2836	1006.4	1047	1052	550
Thermal expansivity, β (K^{-1})	4.5×10^{-4}	–	–	5.8×10^{-7}	9×10^{-6}
Viscosity, μ (kg/m × s)	2.2×10^{-3}	1.789×10^{-5}	–	–	–

Table2
Characteristics of $NaNO_3$ single crystals grown by conventional CZ and AVC-CZ techniques.

	CZ crystal	AVC-CZ crystal
Growth conditions		
Pulling rate, mm/h	10	10
Rotation speed, rpm	6	6
Vibrational frequency, Hz	0	17
Vibrational amplitude, mm	0	0.7
Characteristic		
Dimension (D × L), mm	30 × 50	32 × 45
Dislocation density, cm^{-2}	32	1–2
Rocking curve FMHW, arcmin	22.4	2.3
Microhardness, kg/mm^2	16.2	24.8

numerical simulation proved by physical experiments the flows velocity near the disk increased in three orders of magnitude in AVC activated melts (Fig. 2).

2.2. $NaNO_3$ crystal growth

Sodium nitrate crystals were grown in Czochralski configuration using both conventional CZ and AVC-CZ techniques [2] using extra-pure powder (99.9995 wt.% according to ICP-MS by NexION 300D, Perkin Elmer Inc. see Suppl.). The growth procedure is described in detail in Ref. [10]. $NaNO_3$ single crystals were grown in Czochralski configuration using the seed (5 mm diameter 30 mm length). We started the growth without AVC application, made necking, shoulder portion and cylindrical body. After we grew 20 mm cylindrical body (30 mm diameter) we made necking and applied the AVC. The cylindrical boule (32 mm diameter 45 mm length) was grown at AVC action (A=0.7 mm, f=17 Hz). The growth conditions and crystals' parameters are presented in Table 2.

We grinded the crystals to 15–30 μm size powder to carry out DSC and high-temperature XRD analyses. For the further discussion let's mark them “CZ-P” and “AVC-CZ-P”.

2.3. Differential scanning calorimetry

The thermo gravimetric and differential scanning calorimetric (TG/DSC) analysis was carried out in corundum crucibles using STA 449 F3 Jupiter (Netzsch-Gerätebau GmbH). During the experiment powder samples have been gradually heated at the air flow (50 ml/min) with 10 K/min rate of heating, with no other changing in rate, isotherms and in cooling and for the further we can consider all changing on DSC curves independent of time. For both powder samples the curves were generally identical (Fig. 3). Two endothermic effects were detected. The first one reflect order-disorder transition in solid sodium nitrate (from $R\bar{3}c$ to $R\bar{3}m$) at 275 °C [11], and the other one deals with crystal-melt phase transition (with minimum of the heat effect at ~312 °C). For the both effects onset and offset temperatures, as well as peak temperature and thermal effect are summarized in Table 3.

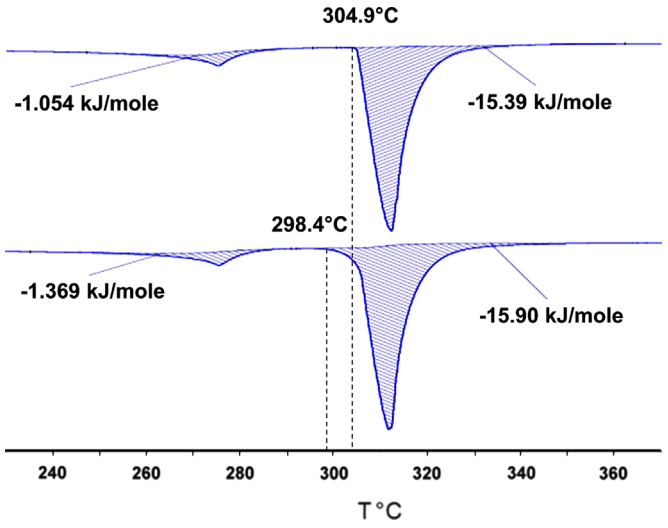

Fig. 3. DSC melting curves of $NaNO_3$ powders made from conventional CZ (top) and AVC-CZ (bottom) grown crystals

2.4. High-temperature XRD-measurements

The powder samples were placed into a quartz glass cell and analyzed by X-ray diffraction was performed with a D8 ADVANCED diffractometer (Bruker GmbH) equipped with high-temperature oven chamber HTK 1200 N (Anthon PAAR GmbH) in (Θ, 2Θ) mode with a copper anode (Cu-Kα, λ=1.5418 Å) 2Θ-scan range, 20–50°, scan step=0.02° and 2 s/step. In the experiment each sample was heated step-by-step from the room temperature to 370 °C with 30 min exposure at the every step 25 °C, 240 °C, 280 °C, 300 °C, 305 °C, 320 °C, 330 °C, 370 °C.

The obtained intensity curves (for the melt) were analyzed to achieve radial density distribution function $\boldsymbol{R(r)}$, reduced intensity function $\boldsymbol{S(K)}$. Expression for the structural factor of liquid $\boldsymbol{\alpha}$, wave vector difference $\boldsymbol{K}$ for the incoming and scattered waves, atomic scattering factors and $\boldsymbol{R(r)}$ and reduced intensity function $\boldsymbol{S(K)}$ were as follows:

$$K = (S - S_0) = 4\pi \sin(\theta/\lambda),$$

$$f(K) = \int_0^\infty 4\pi r^2 \rho(r) \frac{\sin Kr}{Kr} dr,$$

$$\alpha(K) = 1 + \frac{I(K) - \Sigma_i c_i f_i^2}{\Sigma_i c_i f_i^2} = 1 + \int 4\pi r [R(r) - (\Sigma_i c_i n_i)^2 \rho_0] \frac{\sin Kr}{Kr} dr$$

Where

$$n_i^2 = < \frac{f_i^2}{\Sigma_i c_i f_i^2} >,$$

$$R(r) = (\Sigma_i c_i n_i)^2 \rho_0 + \frac{1}{2\pi^2 r} \int (\alpha(K) - 1) K \sin Kr \, dr,$$

$$S(K) = (\alpha(K) - 1) K,$$

here $\boldsymbol{\theta}$ is a half of an angle between these two waves, $\boldsymbol{r}$ – distance from the center of an atom, $\boldsymbol{\rho_0}$- average particle density, concentration of a component $\boldsymbol{I}$. It should be noted, that measured

Table 3
Parameters of DSC melting curves for $NaNO_3$ powder made from AVC-CZ and CZ grown crystals.

Powder initial material	Peak 1 ($R\bar{3}c \rightarrow R\bar{3}m$)				Peak 2 (melting)			
	T_{onset} °C	T_{peak}	T_{offset}	ΔH κJ/mole	T_{onset} °C	T_{peak}	T_{offset}	ΔH κJ/mole
CZ crystal	270.9	275.2	280.7	-1.054 ± 0.095	304.9	312.4	317.2	-15.392 ± 0.016
AVC-CZ crystal	269.7	275.5	281.8	-1.369 ± 0.101	298.4	311.8	318.0	-15.902 ± 0.017

structural factor of liquid α and radial density distribution function $\boldsymbol{R(r)}$ are general values measured for complex (associated) melt of $NaNO_3$. Atomic scattering factors $\boldsymbol{f(K)}$ for each component for $Cu-k_\alpha$ radiation were taken from [12]. Finally we obtained radial density distribution functions for CZ-P and AVC-CZ-P samples at different temperatures (Fig. 4).

3. Results and discussions

In [13] it was demonstrated that at AVC application to the CdTe melt the momentum viscous dissipation energy at the oscillating disk edges could be reached $10^7\ Ws^{-1}m^{-3}$. In the recent cell configuration for $NaNO_3$ melt this value was calculated as $3 \times 10^5\ Ws^{-1}m^{-3}$ at AVC impact ($\boldsymbol{f}$=25 Hz, $\boldsymbol{A}$=0.7 mm) (Fig. 5). The momentum energy which could dissipate in 1 nm^3 is 240 J. In [14] it was demonstrated by molecular dynamic simulation that a disaggregation of 55-parts metal cluster needs 200–600 J/mol. So, the AVC induced energy could be enough for a disaggregation of complex associates in the melt.

The disaggregation process is intensively going in the small area near the disk edge. Furthermore the dissociated particles will spread by flows in all melt volume. Simultaneously, the association process takes place. On Raman spectra for different melts ($NaNO_3$, margarine acid, paraffin mixture) we observed changes in shape and configuration of vibronic peaks depending on AVC activation time at constant temperatures (Fig. 6). These changes could not depend on a melt flow velocity because at a high temperature both AVC-activated and steady melts were characterized by the same Raman spectra (see Fig. 9 −310 °C), while the melt flow velocities for these melts differed more than in an order of magnitude (Fig. 2). Thus, the change in Raman spectrum should be attributed with a change in the melt structure.

The Raman spectra changes were reversible. After the AVC application was turned off the peaks characteristics returned to their natural state for a steady melt at a given temperature.

A typical dependence of structure changes on AVC time was characterized by three parts (Fig. 7). The first part corresponds to the melt structure change up to the certain level. The second part corresponds to the stationary state of the melt determined by the vibrational intensity. The third part after the AVC is switched off reflects the relaxation process in the melt according to its natural thermodynamic state.

In the case of paraffin mixture we found out that the final state of the activated melt depended on vibrational intensity ($\boldsymbol{I}=\boldsymbol{A}\times\boldsymbol{f}^{\boldsymbol{2}}$) but neither on the amplitude nor on frequency separately. The final activated state at a certain temperature reflects full disordering in the melt achieved by the AVC impact. And this is observed for the most of vibronic modes for the analyzed substance. Fig. 8 shows the changes of normalized FWHM(i) towards the highest level of disorder FWHM($_{max}$) *vs* AVC intensity.

This is very important to design industrial AVC systems of different scales and for various chemical compounds. For the need to strongly activate the melt the vibrational frequency ($\boldsymbol{f}$) should be increased. But for the fine adjustment of flows velocity it is better to vary the vibrational amplitude ($\boldsymbol{A}$) due to the higher contribution of the frequency in the vibrational intensity comparing to the amplitude.

Measurement of Raman spectra of AVC-activated and steady melts of sodium nitrate in a narrow temperature range near the melting point showed the shift of the peak maxima, as well as changing the shape of the peak at 1350–1450 cm^{-1} (Fig. 9). A detailed analysis of this peak showed that it could be described by two Gaussians corresponding to v_{10} and v_{14} vibration modes of sodium nitrate [18]. We observed the Gaussians redistribution at temperature increase. The ratio of Gaussian areas characterized a relative melt structure change. We can see that at 310 °C both the AVC-activated and steady melts have the identical peaks. Hence, at 310 °C the structure of these melts is identical. The temperature decrease results to the visible change in the peak's shape. The relative change in the area ratio of Gaussians for the AVC-activated and non-activated melts could be attributed to a degree of melt activation (α)

$$\alpha = \frac{(S_{10}/S_{14}) - (S_{10}/S_{14})_{AHB}}{(S_{10}/S_{14})} = f(T)$$

At α=0 we have a steady non-activated melt. A strongly activated melt is characterized by $\alpha \rightarrow 1$. We observe that α decreases from 0.4 at 306 °C to 0.01 at 310 °C (Fig. 10). At a certain high temperature the equilibrium melt is already dissociated and its activation does not occur. Hence, it is possible to say that this dependence (Fig. 10) demonstrates the degree of AVC activation of melt with temperature.

We supposed that alteration in the melt structure led to the growth of single crystals with different properties. We observed a strong improvement in the quality of AVC grown crystals (Table 2). And we tried to check the popular idea of heritage between solid and liquid phases.

Analysis of the melting process of powders with a different prehistory showed that the AVC-CZ-P sample started to melt at the lower and finished it at the higher temperatures comparing to the CZ-P sample. The melting heat of the conventional powder was 3% less than of the AVC-CZ-P sample.

The low melting temperature of the AVC-CZ-P sample was also proved by high temperature X-ray diffraction experiments (Fig. 4). At 300 °C we observed the AVC-CZ-P sample melting while CZ-P sample stays solid. It could be explained by the difference in energy states of the AVC-CZ crystal and the conventional CZ crystal.

We tried to explain the difference in the melting temperatures of CZ and AVC-CZ crystals. In the both cases the oxygen partial pressure in the growth setup was the same (~0.2 atm). At CZ crystal growth (see Fig. 11 upper left) the thermogravity flows (TC) transfer oxygen from vapor through the melt to the interface. By this way the oxygen chemical potential (μ_o^l) near the interface becomes higher than in the melt volume.

When we apply the AVC the vibrational flows transfer the melt from the volume to the crucible walls. And after then they are moving down the walls and promote leveling of μ_o^l in the whole melt volume. Obviously, in the AVC case $\mu_{o,AVC}^l$ will be less than $\mu_{o,TC}^l$ at conventional CZ growth.

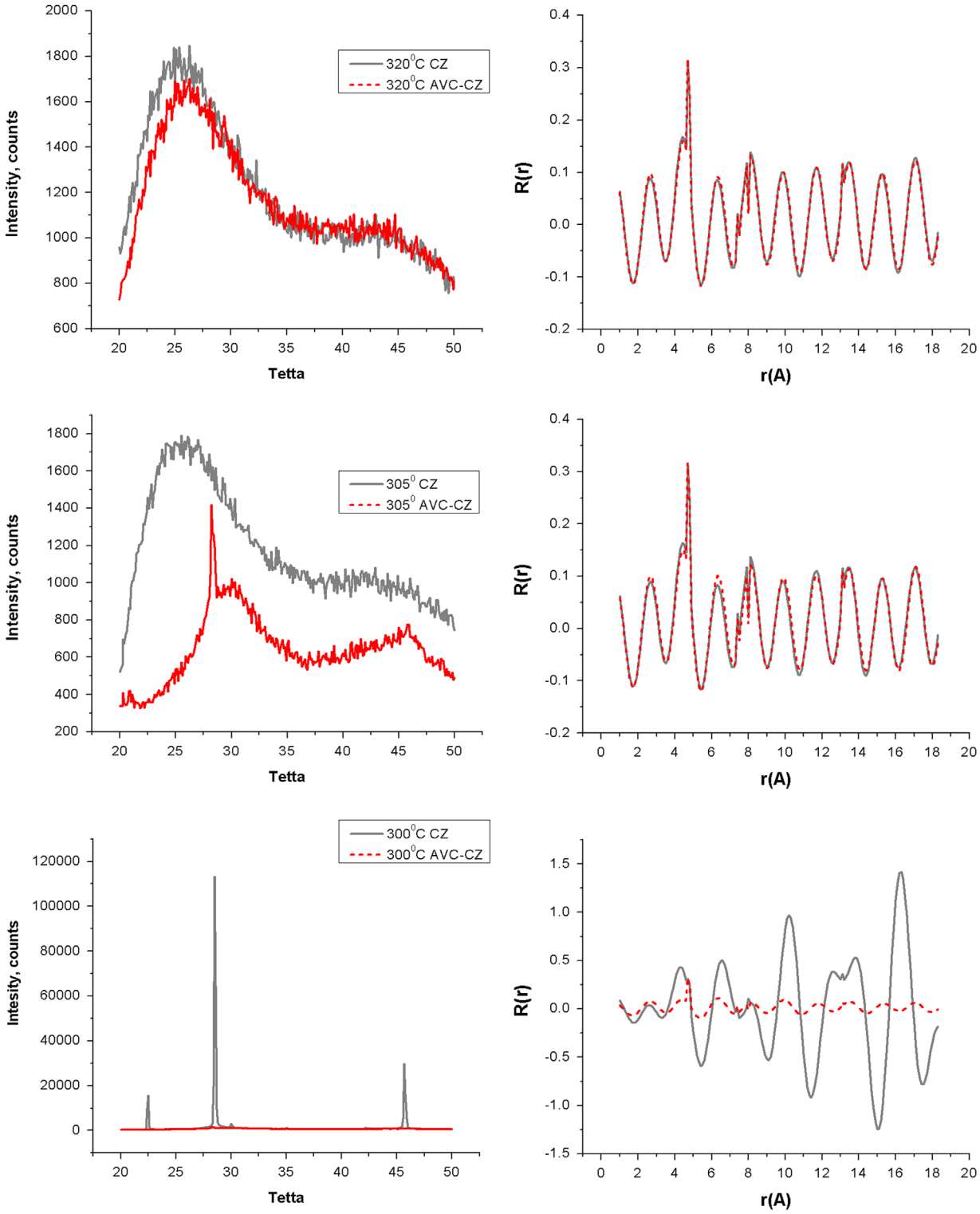

Fig. 4. XRD intensity (left row) and radial distribution function (right row) of $NaNO_3$ powders/melts produced from conventional CZ (top) and AVC-CZ (bottom) grown crystals at different temperatures.

In the stationary state (μ_o^l) will differ from that one in the vapor (μ_o^v) by a constant.

$$\mu_o^l = \mu_o^v + C$$

In our experiments we had $\mu_o^v = const$. It means that

$$\mu_{o,TC}^l = \mu_o^v + C_{TC} > \mu_{o,AVC}^l = \mu_o^v + C_{AVC}$$

$$C_{TC} > C_{AVC}$$

A difference between $\mu_{o,TC}^l$ and $\mu_{o,AVC}^l$ should cause a difference in concentration of over-stoichiometric oxygen in $NaNO_3$ crystals. According to the phase stability rule at a higher oxygen chemical potential a concentration of over-stoichiometric oxygen or sodium vacancies will be higher. There is no information about sodium

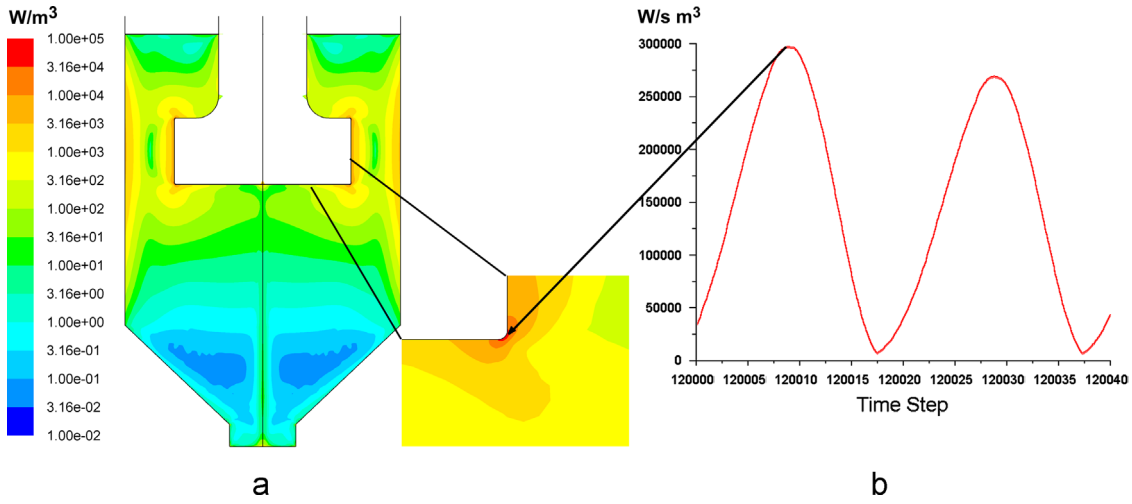

Fig. 5. Numerical simulation of average (*a*) and momentum (*b*) viscous dissipation in AVC activated (***f***=25 Hz, ***A***=0.7 mm) $NaNO_3$ melt.

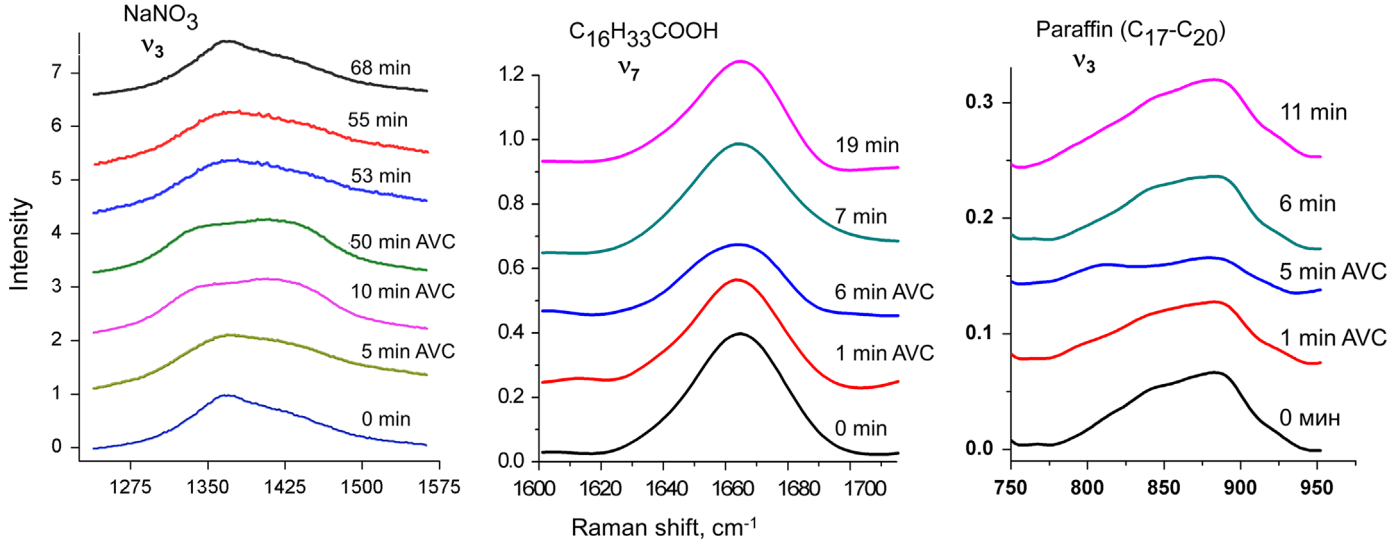

Fig. 6. Peaks of Raman spectrum of melts on AVC activation time: $NaNO_3$ (330 °C), margarine acid (81 °C) and paraffin mixture (C_{17}-C_{20}) (85 °C).

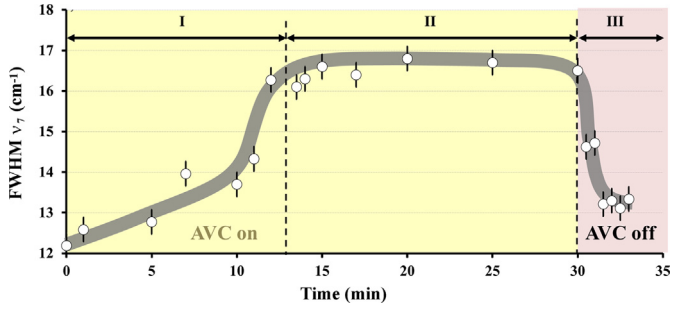

Fig. 7. FWHM of ν_7-peak of Raman spectrum of margarine acid melt AVC activated with ***A***=0.75 mm ***f***=35 Hz at T=81 °C.

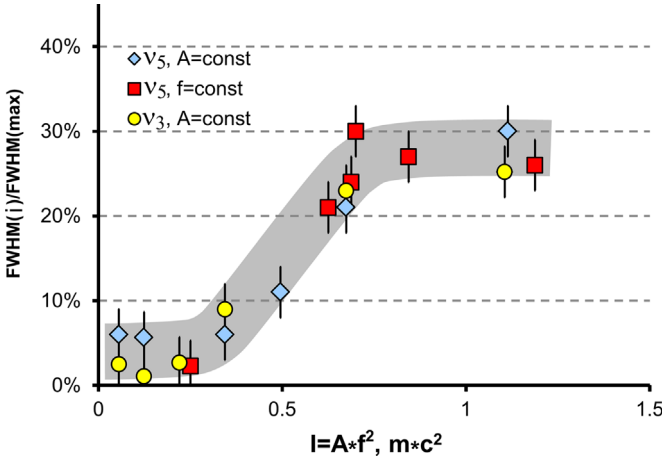

Fig. 8. Effect of AVC activation of paraffin mixture (C_{17}-C_{20}) melt at T=81 °C on FWHM of Raman peaks (ν_3–1080 cm^{-1}, ν_5-1370 cm^{-1}).

nitrate nonstoichiometry mechanism, thus, the both assumptions are equiprobable.

Fig. 11 a,b shows the possible schemes of *T-x* section and μ-*T* projection of sodium nitrate near the melting point. According to the above assumption at the CZ conventional crystal growth (TC mode) the concentration of over stoichiometric oxygen in the crystal will be higher comparing to that one for the AVC-CZ grown crystal due to a higher $\mu^{l}_{0,TC}$ near the interface. According to the scheme (Fig. 11b) in TC mode the $NaNO_3$ crystallization will occur at a higher temperature (T_1) contrary to the AVC mode in which

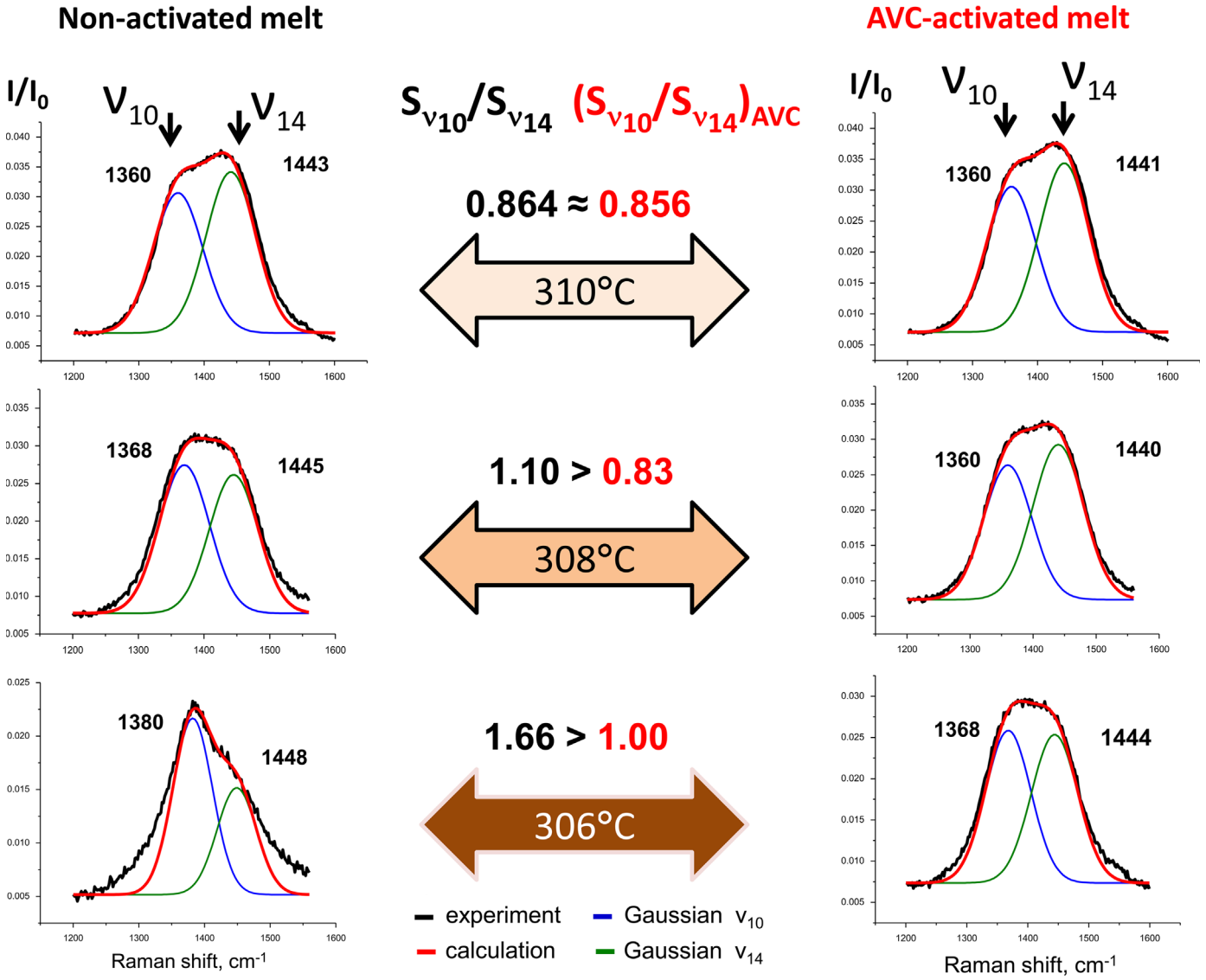

Fig. 9. Decomposition of Raman spectra of non-activated (left column) and AVC activated (right column) $NaNO_3$ melt at different temperatures near the melting point.

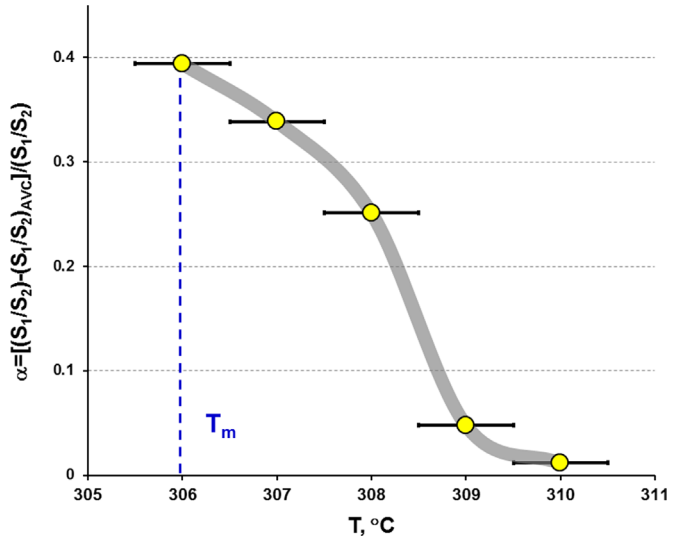

Fig. 10. Temperature dependence of the AVC activation degree of $NaNO_3$ melt based on Raman spectra data.

the crystallization will occur at T_2. It corresponds to μ-T projection when we observe the higher μ_{TC} for T_1.

To prove the above assumption we analyzed $NaNO_3$ crystal's composition by EDAX (Jeol 6510LV scanning electron microscope with EDX analyzer INCA Energy 3D MAX). We found out the oxygen content in the AVC-CZ crystal was 59.84 ± 0.42 mol.% while in the CZ crystal $X_O = 60.90 \pm 0.13$ mol.% (Table 4). So, we experimentally approved the explanation about the difference of melting temperatures of CZ and AVC-CZ crystals as a result of nonstoichiometry difference.

We have tried to summarize the diverse experimental data on the energy state diagram for melts and crystals (Fig. 12). In this diagram the energy scale is relative. Zero state ($E=0$) corresponds to the solid-melt transition. The AVC activated melt according to DTA is characterized by greater energy than the steady melt at the same temperature. On the other hand the AVC grown crystal and the conventional CZ grown crystal are melting with different endothermic effects according to DSC. After the melting of the AVC-CZ grown crystal and the conventional CZ grown crystal the melts' states are identical according to the high temperature X-ray diffraction (see Fig. 4 example for 320 °C).

There are considerable differences not only in the crystallization for steady and AVC melts (4.48 ± 1.79 kJ/mole), but also differences in the melting heats for conventional and AVC

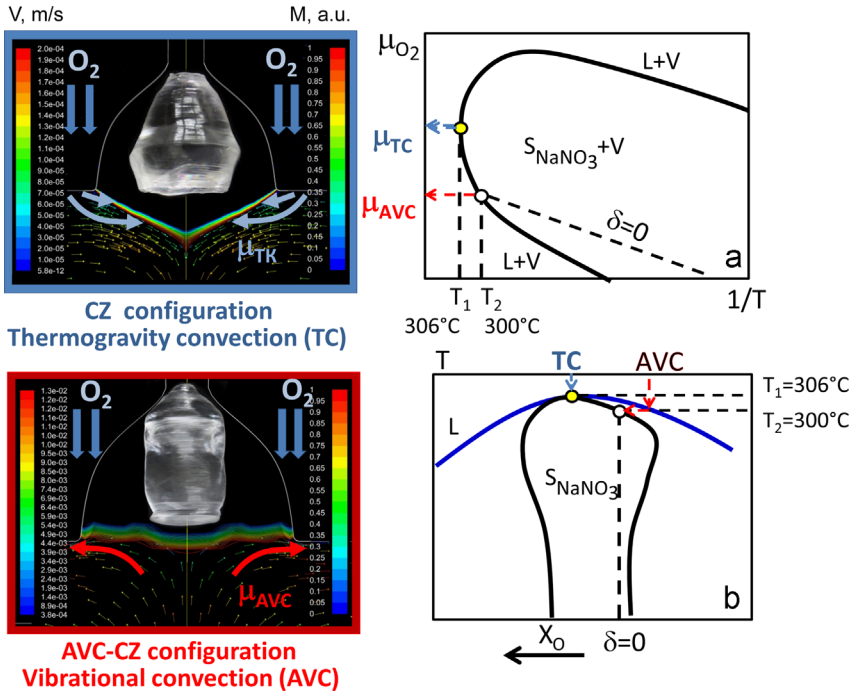

Fig. 11. Sketch of oxygen distribution (left column) at $NaNO_3$ crystal growth by CZ (upper left) and AVC-CZ (bottom left) techniques and the schemes of μ-T projection (a) and T-x section (b) of $NaNO_3$ near the melting point.

Table 4
Composition of CZ and AVC-CZ $NaNO_3$ single crystals by EDAX analysis.

Element	mol.%	
	CZ crystal	AVC-CZ crystal
Na	19.23 ± 0.20	20.08 ± 0.38
N	19.87 ± 0.21	20.07 ± 0.19
O	60.90 ± 0.13	59.84 ± 0.42

9 points measurements were averaged.

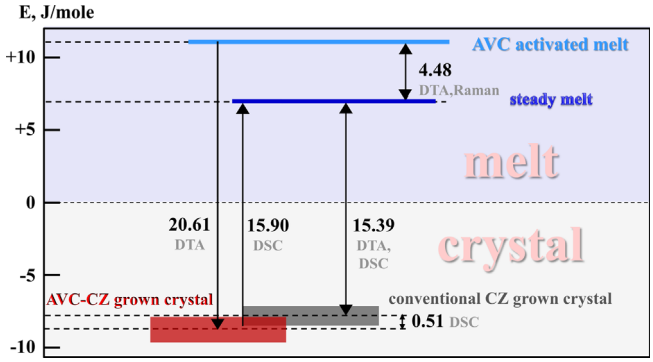

Fig. 12. The energy diagram of $NaNO_3$ states for melt and crystal based on DTA, XRD, DSC and Raman experimental data.

Table 5
Heat effects of crystallization and melting of $NaNO_3$ preparations.

Heat effect	CZ-P or steady melt	AVC-CZ-P or AVC melt	$\lvert\Delta H_{CZ\ S\rightarrow L}-\Delta H_{AVC\text{-}CZ\ L\rightarrow S}\rvert$, kJ/mole
$\Delta H_{S\rightarrow L}$, kJ/mole	−15.902 ± 0.017	−15.392 ± 0.016	0.510 ± 0.033
$\Delta H_{L\rightarrow S}$, kJ/mole [13]	15.73 ± 0.78	20.61 ± 1.01	4.48 ± 1.79
$\lvert\Delta H_{S\rightarrow L}-\Delta H_{L\rightarrow S}\rvert$, kJ/mole	0.17 ± 0.80	5.22 ± 1.03	

crystalline phases prepared from various melts (0.510 ± 0.033 kJ/mole) (Table 5).

With a great caution we can talk that the improvement of structure-sensitive properties of AVC-CZ crystals associated with a disorder decrease, resulted from the reduction of over-stoichiometric oxygen. The lowest energy state of the AVC-CZ crystal (Fig. 12) characterized the crystals with maximal structure perfection which corresponds to low oxygen non-stoichiometry (or close to the stoichiometric composition). This conclusion does not contradict thermodynamic laws, according to which the energy of crystal lattice of an ideal crystal is minimal comparing to the lattice energy of an imperfect crystal [19].

4. Conclusion

It was established that the AVC application changed significantly the melt's properties as an effect of melt activation. AVC technique impact on thermodynamic and structural transformation in complex compound melts, basically, the sodium nitrate melt has been demonstrated. We have summarized information produced by different independent techniques (DTA, DSC, High-temperature XRD, Raman spectroscopy). The single crystals grown from the activated melt showed the unique properties comparing to those ones grown from the steady melt. Moreover, the single crystals grown from the activated melt partially heritage its thermodynamic properties. As a result one can obtained different melting heat values for an extra pure chemical compound depending on its synthesis conditions and nonstoichiometry.

Acknowledgments

The research was financially supported by the Russian Foundation for Basic Research by grants No. 13-02-91377 and 13-02-12199.

Appendix A. Supporting information

Supplementary data associated with this article can be found in the online version at http://dx.doi.org/10.1016/j.jcrysgro.2014.11.022.

References

[1] E.V. Zharikov, Advanced technologies of crystal growth from melt using vibrational influence/in crystal growth technology, in: P. Capper, P. Rudolph (Eds.), Semiconductors and Dielectrics, Wiley-VCH Verlag GmbH & Co. KGaA, Weinheim, Germany, http://dx.doi.org/10.1002/9783527632879 (Chapter 3).

[2] I.Ch. Avetissov, A.P. Sadovskiy, E.A. Sukhanova, G.Yu. Orlova, I.A. Belogorokhov, E.V. Zharikov, Perfection of $NaNO_3$ single crystals grown by axial vibrational control technique in Czochralski configuration, J. Cryst. Growth 360 (2012) 167.

[3] Songming Wan, Xia Zhang, Sijie Zhao, Qingli Zhang, Jinglin You, Hui Chen, Guochun Zhangc, Shaotang Yina, Growth units and growth habit of α-BaB_2O_4 crystal, J. Appl. Cryst. 40 (2007) 725–729.

[4] V.P. Skripov, M.Z. Faizullin, Crystal-Liquid-Gas Phase Transitions and Thermodynamic Similarity, Wiley-VCH Verlag GmBH&Co KGaA Weinheim, 2006 (ISBN: 978-3-527-40576-3).

[5] S. Singh, Phase transitions in liquid crystals, Phys. Rep. 324 (2000) 107–269.

[6] Guang Bao Mi, Jing Xia Cao, Xu Huang, Structure and property of metal melt IV —Evolution of titanium melt residual bond structure and its effect on dynamic viscosity science China physics, Mech. Astron 55/8 (2012) 1371–1375.

[7] Yu.K. Voronko, A.V. Gorbachev, V.V. Osiko, A.A. Sobol, R.S. Feigelson, R.K Route, Study of the boron-oxygen units in crystalline and molten barium metaborate by high temperature Raman spectroscopy, J. Phys. Chem. Solids 54 (11) (1993) 1579–1585.

[8] ANSYS FLUENT Theory Guide Release 14.5 @, SAS IP Inc., 2012.

[9] I. Kh. Avetisov, E.V. Zharikov, A.Yu. Zinov'ev, A.Yu. Mel'kov, A computer-basedfacility for investigating the melt hydrodynamics during Bridgman crystal growth at low-frequency vibrations in a melt, Instrum. Exp. Tech. 47 (2004) 554.

[10] I.Ch. Avetissov, A.P. Sadovskii, E.A. Sukhanova, E.V. Zharikov, A.I. Belogorokhov, B.N. Levonovich, Czochralski crystal growth assisted by axial vibrational control technique, J. Cryst. Growth 312 (2010) 1104.

[11] M.O. Steinitz, D.A. Pink, J.P. Clancy, A.N. MacDonald, I. Swainson, Sodium nitrate — a difficult discontinuous phase transition, Can. J. Phys. 82 (2004) 1097–1107.

[12] International tables for crystallography volume C: mathematical, physical and chemical tables, E. Prince First (Ed.), online edition (2006) doi: 10.1107/97809553602060000103.

[13] I. Avetissov, A. Sadovskiy, S. Belov, A. Khomyakov, K. Rekunov, V. Kostikov, E. Sukhanova, Thermodynamic features of axial vibrational control technique for crystal growth from the melt, CrystEngComm 15 (2013) 2213–2219.

[14] J.P.K. Doye, The Structure, Thermodynamics and Dynamics of Atomic Clusters. Dissertation, Univerisity of Cambridge, Gonville & Caius College (1996) 254 (September).

[15] D.R. Lide (Ed.), CRC Handbook of Chemistry and Physics, CRC Press, Boca Raton, 1990, pp. 4–104 (5-64-7).

[16] D. Schwabe, A. Scharmann, Some evidence for the existence and magnitude of a critical Marangoni number for the onset of oscillatory flow in crystal growth melts, J. Cryst. Growth 46 (1979) 125.

[17] D. Schwabe, A. Scharmann, F. Preisser, R. Oeder, Experiments on surface tension driven flow in floating zone melting, J. Cryst. Growth 43 (1978) 305.

[18] G.R. Wilkinson, Raman Spectra of Ionic, Covalent and Metallic Crystals, in: A. Anderson (Ed.), The Raman Effect, vol. 2, Marcel Dekker, New York, 1971, pp. 812–983 (especially the section on alkali nitrates, pp. 911–916).

[19] F.A. Kroger, The Chemistry of Imperfect Crystals, North-Holland Pub. Co.; New York, Interscience Publishers, Amsterdam, 1964.